



Modal variability in the Southeast Pacific Basin: Energetics of the 2009 event



Wilbert Weijer*

Los Alamos National Laboratory and the New Mexico Consortium, Los Alamos, NM, United States

ARTICLE INFO

Available online 17 October 2012

Keywords:

Dynamical Oceanography
Ocean circulation
Bottom topography effects
Abyssal plains
Regional: Southeast Pacific Ocean
Bellingshausen Basin

ABSTRACT

We study the barotropic variability in the Southeast Pacific Basin, in particular focusing on the extreme event during the fourth quarter of 2009. A 3-year integration of a barotropic shallow-water model forced with wind stress anomalies generates localized variability that is similar in spatial extent and amplitude as the observed anomalous event. An eigenmode analysis of the same model shows the presence of several free modes in the Southeast Pacific, but projection of the modal patterns on the model output shows that their amplitudes are low. Instead, the mode is interpreted as an *almost-free* mode. The modal excitation accounts for a considerable fraction (23% on average) of the kinetic energy input by the wind stress in the Southeast Pacific Basin, increasing to 38% for the anomalous event in 2009. Surprisingly, a similar but weaker event during the third quarter of 2008 appears to have been more significant from an energetics point of view, with almost 50% of the energy being input into the mode. Key areas of energetic dissipation appear to be the Eltanin Fracture Zone, the crest of the East Pacific Rise, and the Chile Rise/East Pacific Rise intersection.

© 2012 Elsevier Ltd. All rights reserved.

1. Introduction

Several ocean basins exhibit significant barotropic variability on intraseasonal scales (Chao and Fu, 1995; Fu and Smith, 1996; Fu, 2003; Vivier et al., 2005). Specific areas in the Southern Ocean with significantly enhanced levels of sea surface height (SSH) variability are the Australian–Antarctic Basin (Webb and De Cuevas, 2002a; Weijer et al., 2009; Weijer, 2010), the Argentine Basin (Fu et al., 2001; Hughes et al., 2007; Weijer et al., 2007a), and the Bellingshausen Basin (Webb and De Cuevas, 2002b, 2003). These basins are characterized by contours of potential vorticity f/H (where f is the Coriolis parameter and H is the water depth) that are closed or almost closed around isolated bathymetric features, like abyssal plains, ridge segments or large seamounts.

In principle, circulation along closed contours of f/H , is free in the sense of being unconstrained by vorticity dynamics, and once excited, is damped mainly by frictional effects (Koblinsky, 1990). In practice, however, also flow along *almost* closed contours of f/H can be excited, termed *almost-free* modes by Hughes et al. (1999), who used this concept to describe a band of enhanced SSH variability around Antarctica. Rather than being damped by friction, the circulation loses most of its energy to waves at a few choke points, where the flow has to cross contours of f/H to complete the circuit. This leads to a decay time on the order of

days (Webb and De Cuevas, 2003), compared to several weeks for purely free modes (Weijer et al., 2009). In two recent studies (Weijer et al., 2009; Weijer, 2010) it was shown that the strong intraseasonal variability in the Australian–Antarctic Basin can be ascribed mostly to such an almost-free mode, with a smaller contribution from purely modal circulation.

The potential significance of these modes is that it provides a direct route via which wind energy can be dissipated through interaction with bathymetry. In particular, Weijer (2010) showed that the almost-free mode in the AAB loses a significant fraction of its energy at the apex of the Wilkes Abyssal Plain, both to bottom friction, as well as to wave generation.

Recently, Boening et al. (2011) described an exceptional episode in the Southeast Pacific Basin: during the fourth quarter of 2009 a persistent anomalous anti-cyclonic circulation was recorded in SSH and bottom pressure (BP) records that was unprecedented for the entire lengths of the observational records. A link was made between the excitation of this mode and an anomalously strong and persistent high pressure anomaly, which may have been related to an anomalous Central Pacific El-Niño event (Lee et al., 2010). This link is significant, because of the apparent recent change in the recurrence frequency of Central Pacific El-Niños, compared to the traditional eastern Pacific variety (Ashok et al., 2007).

In this paper we study the dynamics and energetics of the 2009 event in the Southeast Pacific Basin (Fig. 1). In particular we address (i) to what extent the anomalous circulation can be ascribed to free and almost-free topographically trapped modes, and (ii) what this implies for the energetics of the

* Tel.: +1 505 667 7469; fax: +1 505 667 5921.
E-mail address: wilbert@lanl.gov

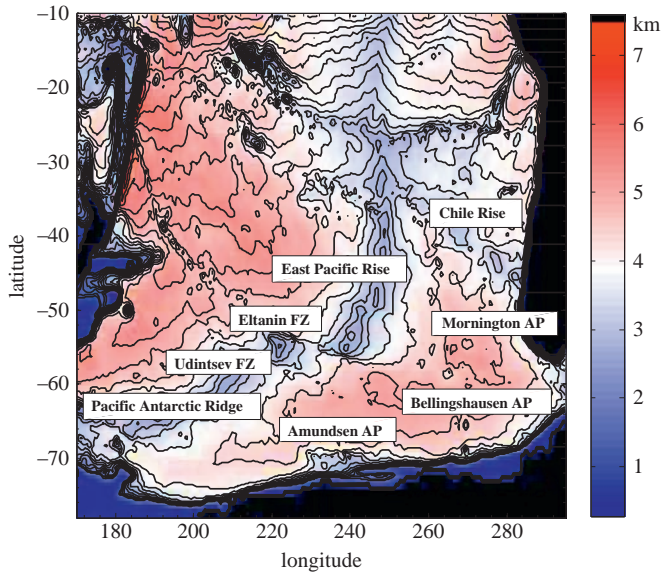


Fig. 1. Bathymetry of the South Pacific (shading, in km depth) with some relevant geographic features (FZ=Fracture Zone; AP=Abyssal Plain). Contours are isolines of $^{10}\log(|f|/H)$, plotted for the interval $[-9.0, -7.0]$ with step 0.05.

barotropic circulation in the Southeast Pacific Ocean. To that end, we perform a normal mode analysis on a shallow-water model of the South Pacific, and perform time-integrations with the same model, to study modal/non-modal energetic interactions.

2. Method

The code used here is based on the shallow-water model introduced by Dijkstra and Molemaker (1999), Dijkstra et al. (1999), and Dijkstra and De Ruijter (2001), modified to account for bathymetry, and used to study topographically trapped variability by Weijer et al. (2007a,b, 2009) and Weijer (2008, 2010). The shallow-water model is configured for the region $[170^{\circ}\text{E}, 295^{\circ}\text{E}]$, and $[78^{\circ}\text{S}, 10^{\circ}\text{S}]$, with a spatial resolution of 0.5° . Bathymetry is based on the ETOPO-2 dataset, interpolated onto the model grid, and smoothed once with a 1-4-1 smoother. Maximum depth is 7600 m. As in Weijer et al. (2009), horizontal viscosity A_h is set at $3 \times 10^3 \text{ m}^2 \text{ s}^{-1}$, with a linear bottom friction coefficient $r = 2 \times 10^{-7} \text{ s}^{-1}$ ($1/58 \text{ day}^{-1}$).

Coefficients of horizontal eddy viscosity are poorly constrained in the ocean, and range from $5 \times 10^3 \text{ m}^2 \text{ s}^{-1}$ (Munk, 1950) to $50 \text{ m}^2 \text{ s}^{-1}$ (Polzin, 2010). In most numerical studies, the value is chosen so that the Munk scale is resolved. With the value used here, this scale is resolved by at least two grid points only south of 56°S , and is hence marginally sufficient. Estimates of bottom friction range from $1 \times 10^{-7} \text{ s}^{-1}$ (Nowlin, 1967) to $5 \times 10^{-6} \text{ s}^{-1}$ (Hirose et al., 2001), and the value used here is at the lower end of this range. To test the robustness of the results with respect to this parameter choice, we repeated the time integration with the values $A_h = 3 \times 10^2 \text{ m}^2 \text{ s}^{-1}$ and $r = 1 \times 10^{-7} \text{ s}^{-1}$.

Wind forcing is derived from the Cross-Calibrated Multi-Platform (CCMP) Ocean Surface Wind Velocity, which is available from 1987 onward (Atlas et al., 1996, 2011). The data are provided 6-hourly on a 0.25° grid. We use the 10 m wind fields from January 1, 2008, through December 31, 2010. First, the wind velocities are converted to wind stress using the Large and Pond

(1982) relation. Then the 6-hourly vector fields are averaged to daily values, the annual and semi-annual cycles are removed, and the data are detrended. Despite removal of the *mean* seasonal cycle, the variance of the wind stress still displays strong seasonality.

The shallow-water model is used to calculate normal modes of the Southeast Pacific barotropic circulation. As in our previous studies, the Jacobi–Davidson QZ (JDQZ) method is used to solve the generalized eigenvalue problem (Sleijpen and van der Vorst, 1996; van Dorsselaer, 1997; Dijkstra et al., 2001), along with the MRILU method for preconditioning the sparse numerical systems (Botta and Wubs, 1999; Dijkstra et al., 2001). In addition, the same model is integrated forward in time for a full 3 years (1096 days), using a Crank–Nicolson time stepping scheme with a 15 min time step. Daily averages of sea surface height (SSH, or η), and the zonal (u) and meridional (v) velocity components are saved.

3. Results

3.1. Time integration

Fig. 2 shows the mean SSH from the shallow-water model for the last 3 months of 2009, which corresponds to the time period for which Boening et al. (2011) found the largest anomalies in SSH and bottom pressure. The model clearly reproduces the large ($O(0.1 \text{ m})$) anomalies in the Southeast Pacific Basin (roughly between 230°E and 280°E (80°W – 130°W), and 65°S and 35°S) that is evident from the bottom pressure and SSH observations.

SSH anomaly time series averaged over the 90°W – 140°W , 55°S – 35°S region are shown in Fig. 3a for comparison with Fig. 1e of Boening et al. (2011). Maximum monthly values reach

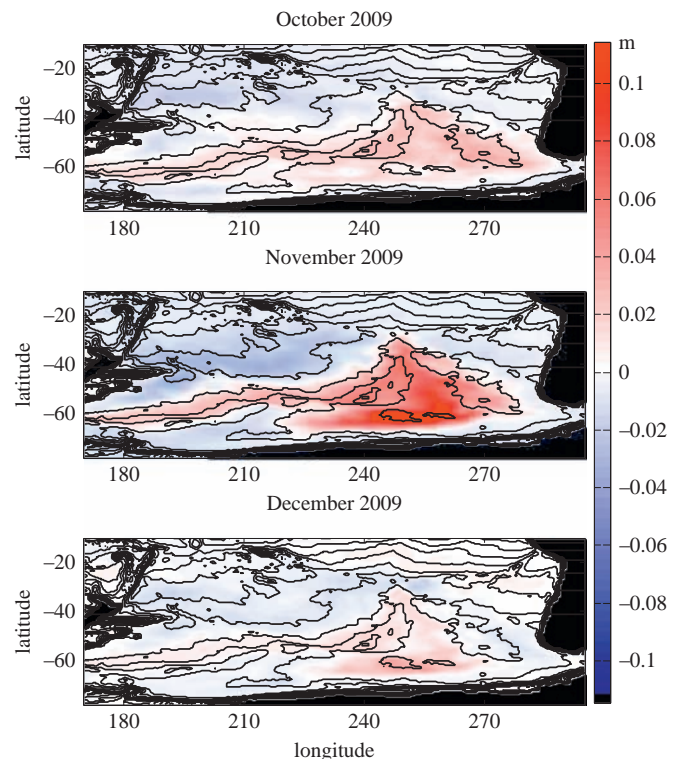


Fig. 2. Average SSH (m) for the months of October, November and December 2009.

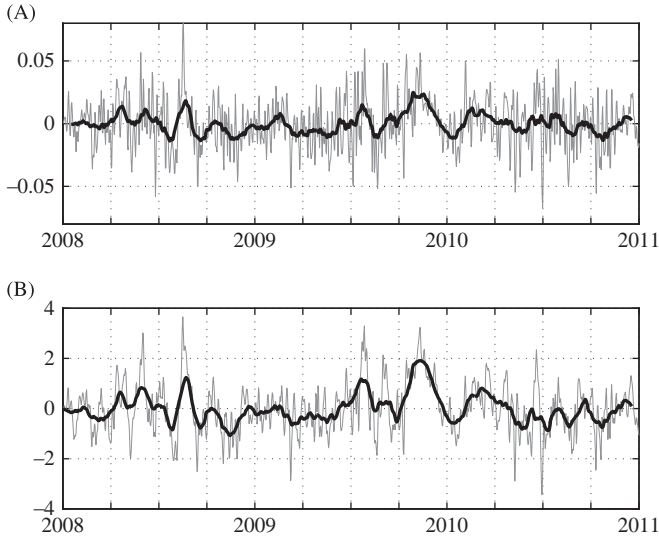


Fig. 3. (a) SSH anomalies averaged over the same region as in Fig. 1e of Boening et al. (2011), i.e., 90°W–140°W, 55°W–35°S. (b) Time series (principal component) of the dominant EOF of η . Black lines indicate 31-day running means.

an amplitude of 0.025 m during the last quarter of 2009 (Q4 2009), while daily values exceed 0.055 m. Boening et al. (2011) find monthly values of about 0.05 m. In addition, our analysis finds significant anomalies during the third quarter of 2008 (Q3 2008), with monthly values topping out at 0.018 m, but with daily peak values of 0.08 m. In Boening et al. (2011), only their ocean bottom pressure record shows an anomaly during that time frame of about 0.03 m. Their model integration shows a peak in Q2 of 2008 instead, which is not matched by the observations. Overall, our model appears to underestimate the amplitude of the anomalous SSH events as found in observations.

An Empirical Orthogonal Function (EOF) analysis is performed on the daily fields of η . The dominant Principal Component (PC; Fig. 3b) accounts for 52% of the variance. It displays considerable synoptic and intraseasonal variability that clearly matches the time series of area-averaged η shown in Fig. 3a. In particular, it reproduces the period of anomalously positive values during Q4 2009: its 2-std excursion corresponds to a 0.08–0.09 m anomaly in η , consistent with the observational results of Boening et al. (2011). Although anomalies with higher amplitude are present in our daily time series (for instance during Q3 2008), the 2009 event is unique in its duration and persistence.

The dominant EOF (Fig. 4) confirms that most of the SSH variance occurs in the Southeast Pacific Basin, as suggested by the observations. Its spatial pattern is clearly governed by the particular distribution of f/H generated by the East Pacific Rise on the northwestern flank, and the Mornington, Bellingshausen, and Amundsen Abyssal Plains on the east and south. As Fig. 4 shows, specific contours of f/H that are only a few degrees apart just east of the Southeast Pacific Basin (for instance, with values of $-10^{-7.48} \text{ m}^{-1} \text{ s}^{-1}$ (blue) and $-10^{-7.60} \text{ m}^{-1} \text{ s}^{-1}$ (cyan)) are separated by almost 40° latitude at 245°E (115°W).

Regression of the corresponding PC onto the velocity components provides a consistent picture of this statistical mode of variability (Fig. 4): it shows that a positive SSH anomaly is associated with southward flow on the western flank of the anomaly (mainly along the crest of the East Pacific Rise), eastward flow in the southern part of the basin, and northward flow in the eastern sector.

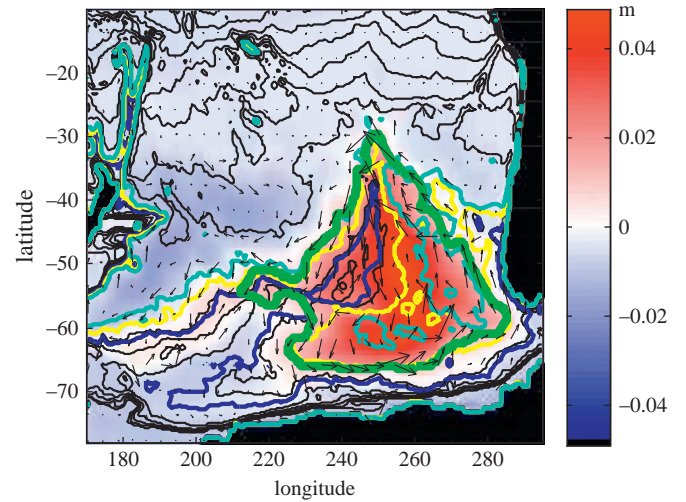


Fig. 4. Dominant EOF of sea surface height (η) variability (shading; represents standard deviation in m), and the regression of the corresponding PC on the velocity fields (vectors; plotted every eighth grid point, or 4°, for clarity). The EOF is renormalized so that the loadings represents the standard deviation, and the PC time series has unit variance. Black contours are isolines of $^{10} \log(|f|/H)$ (plotted for the interval $[-9.0, -7.0]$ with step 0.1); highlighted contours denote values of -7.48 (blue), -7.56 (yellow), and -7.60 (cyan), while the green contour denotes the modal region, defined here as the area where the standard deviation of EOF 1 exceeds 0.01 m.

3.2. Free modes

In this section we address whether free barotropic modes exist in the Southeast Pacific, and whether they account for a significant fraction of the variability in that basin. Fig. 5 shows the result of an eigenmode analysis performed with the same shallow-water model that was used for the time integration. Four stationary modes are found that have a significant expression in the Southeast Pacific. Decay time scales are close to 16 days for all modes. Several of these modes have expressions in different subregions and apparently mix different localized modes. Since the system is fully linear, we can rotate the modes to obtain modes that have a more localized expression. Fig. 6 shows the result of a manual rotation that was found to optimize the local character of the modes. Rotated mode 1 has a dominant expression in the Amundsen and Bellingshausen Abyssal Plains, mode 2 in the northern part of the Southeast Pacific Basin, mode 3 in the Mornington Abyssal Plain region, and mode 4 on top of the East Pacific Rise. These rotated modes will be used in the subsequent analysis.

To study whether these modes truly play a role in the variability in the model, we project the spatial patterns of the modes ($m_i = (m_i^u, m_i^v, m_i^w)$) onto the daily-averaged model fields. The projection time series are shown in Fig. 7. As argued by Weijer et al. (2009), the projection time series based on SSH (γ^{η}) may be less reliable than those based on the velocity components ($\gamma^{uv} = (\gamma^u + \gamma^v)/2$), since the monopolar patterns of m^i make them less scale selective than the generally bipolar patterns of m^u and m^v .

Fig. 7 shows that γ^{η} yields maximum amplitudes for all of modes 1, 3 and 4 during Q4 2009 with very persistent positive amplitudes. Mode 2 does not have a significantly enhanced expression in SSH during this period. Other significant events are Q3 2008 (modes 1 and 4) and Q3 2009 (modes 1 and 3). The projection time series γ^{uv} are smaller in amplitude than γ^{η} by about a factor of 3; they display similar strong positive values for

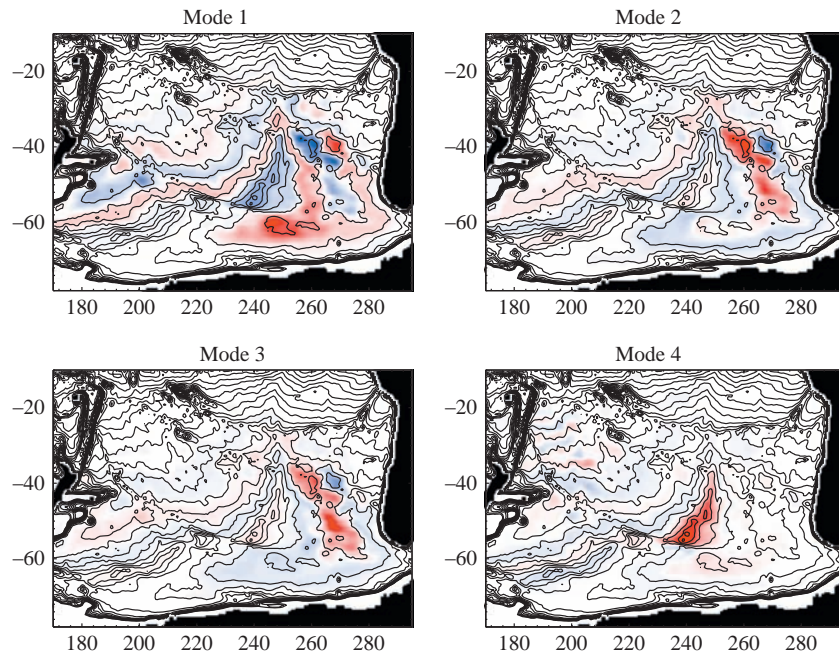


Fig. 5. Four eigenmodes with significant SSH expression in the Southeast Pacific. The amplitude of these eigenmodes is unconstrained, but assumed to be infinitesimally small.

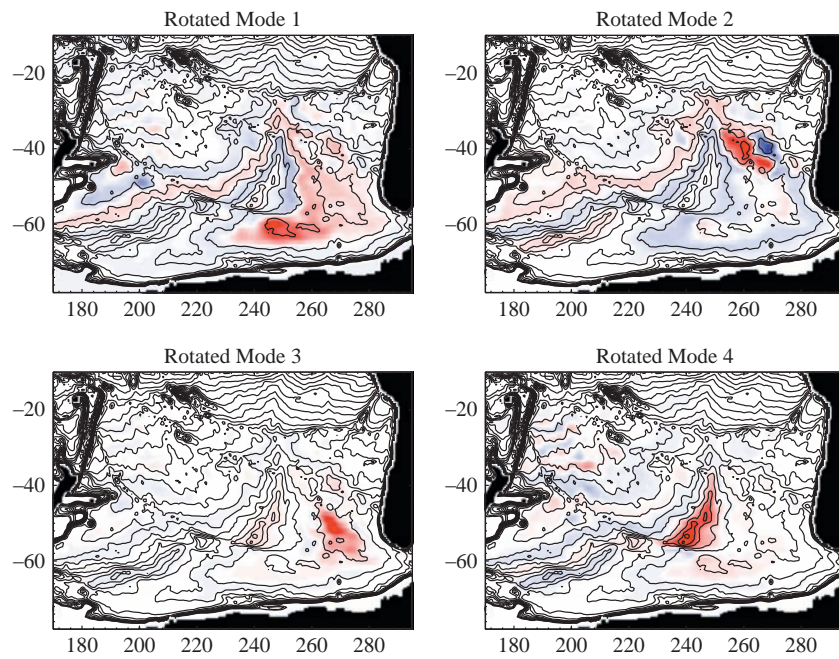


Fig. 6. Four modes after manual rotation of the eigenmodes in Fig. 5.

modes 1 and 3 during Q4 2009, but do not show a significant signal for modes 2 and 4. In addition, mode 1 has equally strong expressions during Q3 2009 and Q3 2010, in both cases accompanied by strong opposing amplitudes of mode 4. The period Q3 2008 is characterized by positive amplitudes of modes 1 and 4, in line with γ^H .

Fig. 8 shows the decomposition of the SSH field (averaged over the Q4 2009) into a purely modal contribution based on γ^{uv} and a residual. Over the entire 3-year length of the time series, the modal projection accounts for little (0.5%) of the mean variance of

SSH. This suggests that free topographically trapped modes play a negligible role in the 2009 event.

3.3. Almost-free mode

3.3.1. Energetics

Following the analysis of Weijer (2010), we assume that the statistical mode in Fig. 4 to some extent reflects the stochastic excitation of an almost-free topographically trapped barotropic mode, and that the amplitude of this modal, or spatially coherent

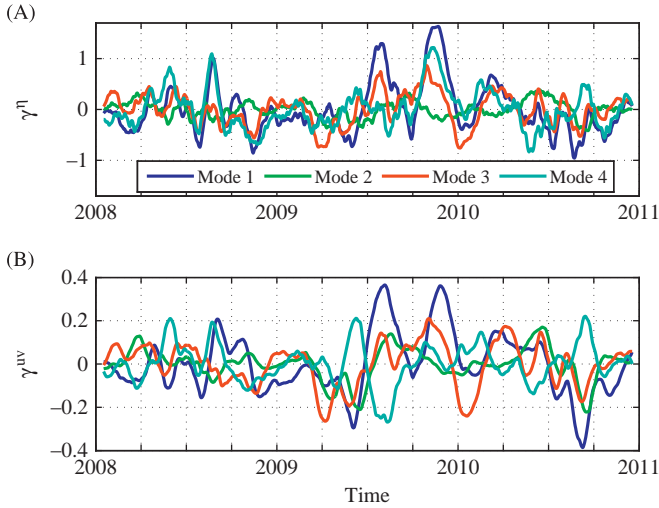


Fig. 7. Projection time series based on the patterns of (a) SSH and (b) the velocity components. Plots show 31-day moving average of the daily time series.

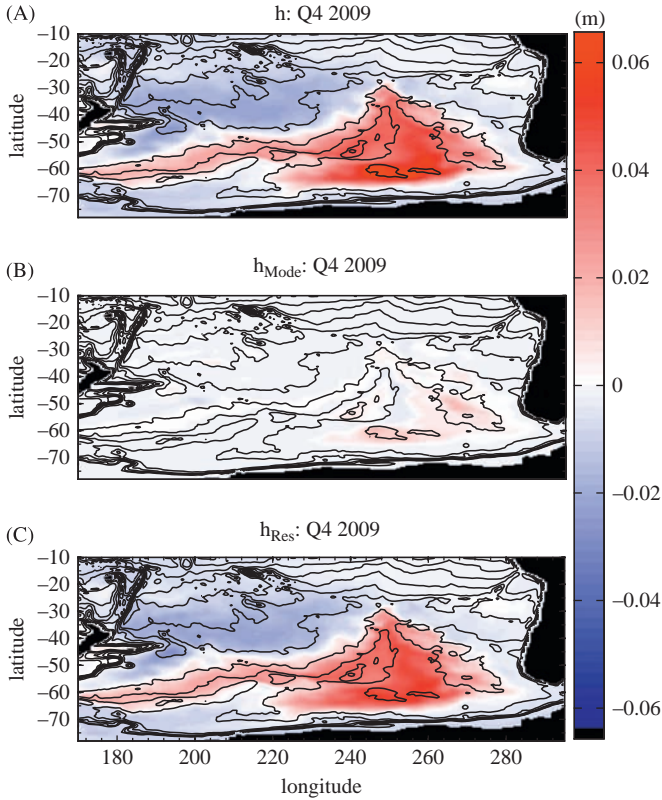


Fig. 8. Decomposition of (a) mean SSH for Q4 2009 into (b) a modal and (c) a residual contribution. Reconstruction is based on γ^{uv} .

circulation pattern can be determined by projection of the modal velocity field on the instantaneous velocity fields. To study the energetics of this mode, we run the simulation once again, but now decomposing the velocity field \mathbf{u} into a modal \mathbf{u}_m and non-modal, residual \mathbf{u}_r , contribution at each time step. Based on this decomposition, the kinetic energy balance can be determined for both the modal and residual velocity fields, as outlined in the Appendix. In particular, we have approximately the following

balances:

$$\frac{dE_m}{dt} = W_m + F_m + R_m \approx 0, \quad (1a)$$

$$\frac{dE_r}{dt} = W_r + F_r + R_r \approx 0. \quad (1b)$$

Here, input of kinetic energy by wind stress forcing is indicated by W , local dissipation due to friction by R , while the residual F , which we will refer to collectively as pressure work, represents other mechanisms of energy transfer. This term contains contributions from (i) the Coriolis term: specifically, spurious work done by the Coriolis force due to discretization errors, and energy exchange between modal and residual circulation through coupling via the Coriolis force; and (ii) pressure gradient forces. This pressure work term, proportional to $-\mathbf{u} \cdot \nabla \eta$, can be rewritten as $-\nabla \cdot \mathbf{u} \eta + \eta \nabla \cdot \mathbf{u}$. The first term is the divergence of energy flux $\mathbf{u} \eta$, which represents transfer of energy to the wave field. The second term represents exchange with potential energy, which is small on the time scales considered here. In addition, there is again energy exchanged between modal and residual circulation, to the extent to which the residual circulation needs to counteract the modal flow field, $\mathbf{u}_r = -\mathbf{u}_m$. These terms are diagnosed during a repeat integration, and their temporal averages are written out at 10-day intervals. Subsequently, the fields are integrated over the modal area, defined here as the region where the dominant EOF exceeds a 0.01 m standard deviation (indicated by the green line in Fig. 4).

3.3.2. Forced integration

The work done by the terms in Eq. (1), integrated over the modal area, show several interesting features (Fig. 9). First of all, the residual circulation (dashed lines) receives most energy from the winds (blue), which is mostly dissipated locally by friction (black). Despite the fact that the seasonal cycle was removed from the wind stress, the seasonal cycle in its variance accounts for the strong seasonality in energy input. In addition, the residual circulation gains kinetic energy from pressure work (red), which can be imported by waves from outside the modal region, or can result from energy conversions with the mode itself.

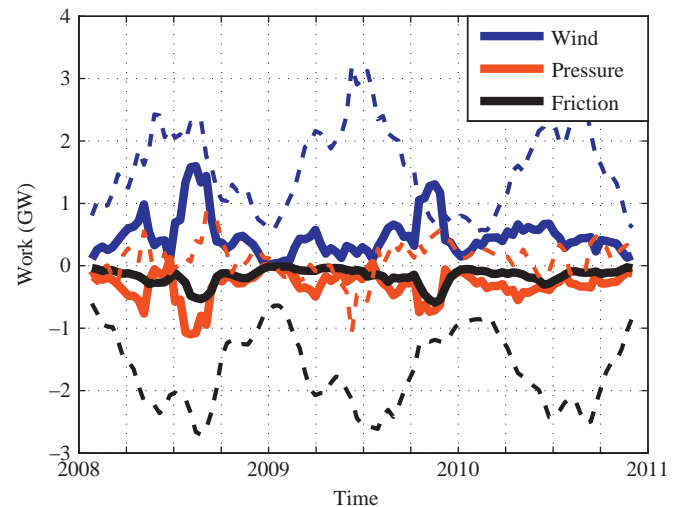


Fig. 9. Energy balance of the modal (solid) and non-modal, residual (dashed) circulation, according to Eq. (1), integrated over the modal area. Time series are 50-day moving averages.

The modal circulation (solid lines) is energized by the wind stress as well. Averaged over the 3-year period, 23% (0.46 GW) of the wind energy input into the modal region is used to energize the mode. The modal circulation loses this energy to friction (0.16 GW, or 34%) and pressure work. This energy is either radiated away to areas outside the modal region, or converted to energy of the residual circulation. A significant anticorrelation (-0.36) between the modal and residual pressure work time series (50-day moving averages) suggests that such a conversion of energy plays an important role, as it does for the Australian–Antarctic Basin (Weijer, 2010).

An interesting, and puzzling result is that the energy input into the modal circulation is stronger during Q3 2008 (1.13 GW) than during Q4 2009 (0.81 GW), despite the distinctively stronger amplitude and longer persistence of the mode during the 2009 period (Fig. 3). Based on this analysis, the 2008 event seems to be more significant from an energetics point of view than the one in 2009.

The spatial distribution of the energy conversion terms for these periods are shown in Figs. 10 and 11. First of all, the mode receives a considerable fraction of the overall energy input into the modal area during these periods (1.13 GW, or 38% for Q3 2008; 0.81 GW,

or 49% for Q4 2009); this is not counting a significant amount of energy that is input outside what is defined here as our modal area, and despite the fact that there is an area on top of the East Pacific Rise where wind forcing *removes* energy from the mode. Here pressure work needs to add energy in order to retain the spatial coherence of the modal circulation.

For Q3 2008, 68% of this energy put into the modal circulation is released by pressure work, while this fraction is 56% in 2009. The residual circulation gains most of its energy due to pressure work over the Eltanin Fracture Zone, over the crest of the East Pacific Rise, and at the Chile Rise/East Pacific Rise intersection, regions where also frictional dissipation is strongest. Apparently, these regions are critical choke points for the modal circulation, as locally strong gradients in bathymetry exist that force the modal circulation to cross isolines of f/H .

The fraction of the modal energy that is locally dissipated by friction is with 44% much higher for Q4 2009 than for Q3 2008 (32%). A possible explanation is that the winds during the 2009 event more efficiently excited the free topographically trapped modes, as shown by Fig. 7, although the apparent smallness of their overall contribution (Fig. 8) casts this explanation in doubt.

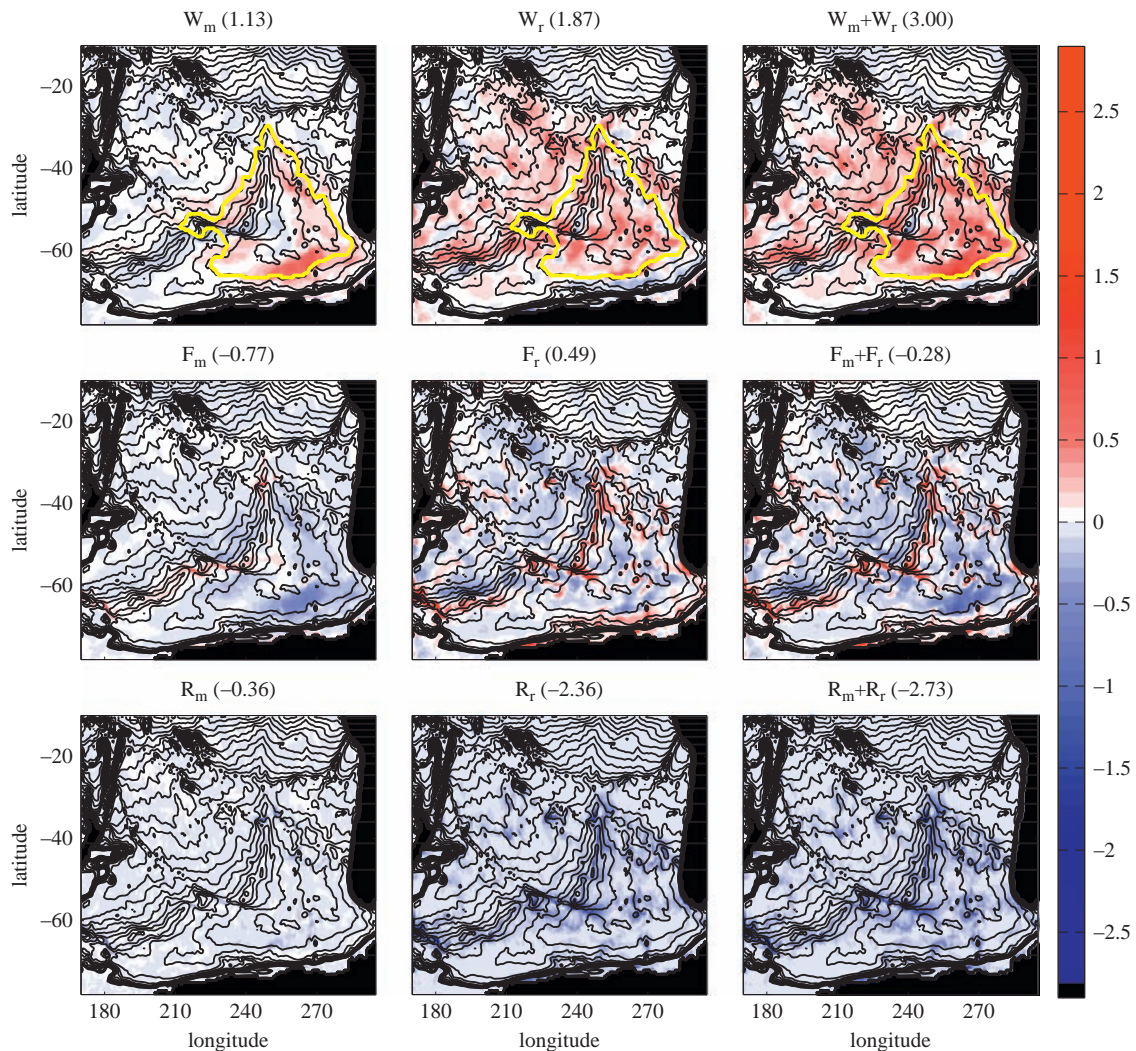


Fig. 10. Terms in the balance of kinetic energy Eq. (1) averaged over Q3 2008 (in m W m^{-2}). Numbers in brackets denote integrals (in GW) over the modal area. This area is indicated by the yellow line in the upper plots. See text for details.

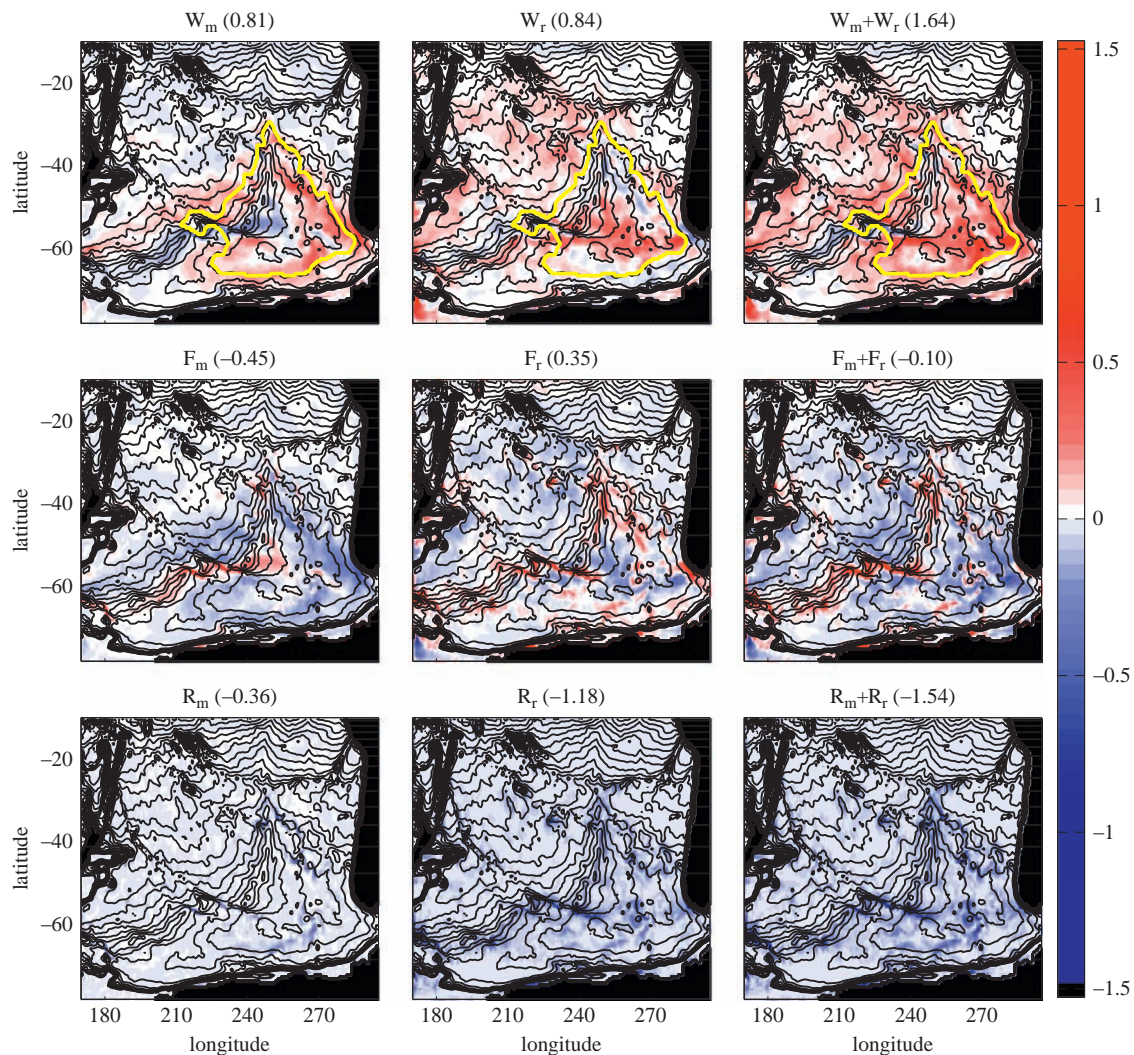


Fig. 11. As Fig. 10, but now for Q4 2009.

3.3.3. Unforced decaying integration

A complementary view of the energy conversions is obtained from an unforced integration, which was initialized with the modal velocity field (at arbitrary amplitude). Fig. 12 shows the energy conversions averaged over the first 6 days of the integration. The mode loses 78% of its initial energy to pressure work, which energizes the residual velocity field. The main areas of energy conversion are the Eltanin Fracture Zone, the crest of the East Pacific Rise, and the Chile Rise/East Pacific Rise intersection, confirming the conclusions based on the forced simulation.

3.3.4. Dependence on frictional parameters

To study the dependence of these results on the frictional parameters used, we reduced horizontal viscosity by an order of magnitude ($3 \times 10^2 \text{ m}^2 \text{ s}^{-1}$) and bottom friction by a factor of 2 ($1 \times 10^{-7} \text{ s}^{-1}$), and repeated the integration and energetics calculations. The overall results are surprisingly robust, as most metrics are almost indistinguishable from the standard run. This confirms that friction, to lowest order, does not play a role in the dynamics of the modal excitation and decay. For instance, energy input by the wind during Q3 2008 is almost identical (3.04 GW vs. 3.00 GW for the standard run), as is the fraction contributed to the modal circulation (39% vs. 38%). However, for the low

frictional values only 11% (vs. 32%) is locally dissipated by friction, while 89% (vs. 68%) is expended on pressure work.

4. Discussion and conclusions

Topographically trapped modal circulations in the oceans can be relevant for focusing wind energy towards a few selected regions, or choke points, where it can be dissipated. This study shows that wind stress events in the Southeast Pacific Ocean can excite an almost-free, topographically trapped barotropic mode that covers the entire Southeast Pacific Basin. Also free modes are excited, but their amplitude is small. An analysis of the energetics of the mode shows that averaged over the 3-year period considered here, 23% (0.46 GW) of the wind energy input into the region is expended on the mode, but this percentage rises to 38% and 49% for the specifically energetic periods of Q3 2008 and Q4 2009. Despite the longer persistence of the Q4 2009 event, the Q3 2008 seems to have been more significant from an energetics point of view.

The crest of the East Pacific Rise, the Eltanin Fracture Zone, and the intersection of the Chile and East Pacific Rises appear to be regions where the mode expends most of its energy. Here the strongest frictional dissipation takes place as well, making these regions specifically interesting for deep ocean mixing. Although

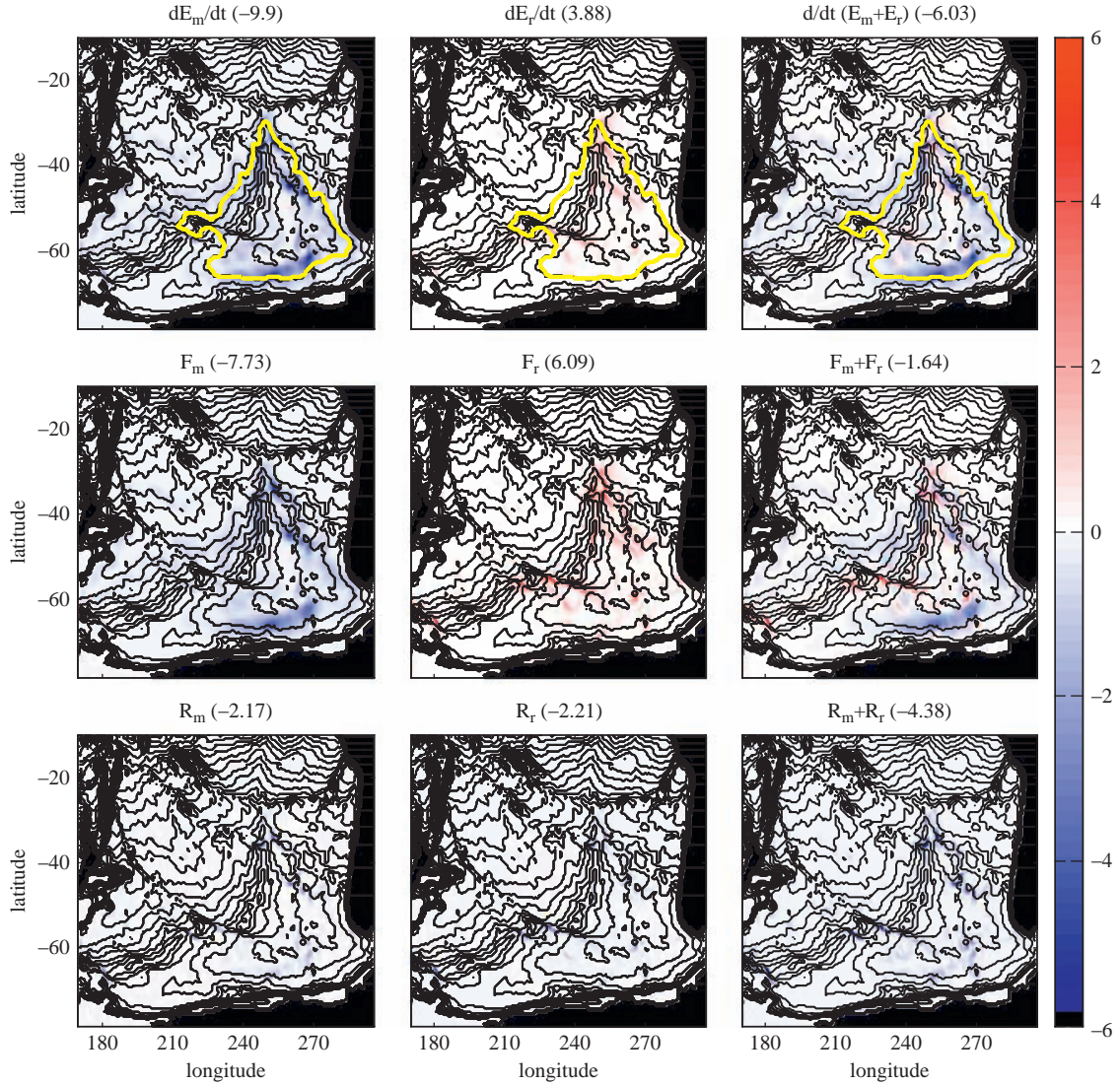


Fig. 12. As Fig. 10, but now showing the energetics of an unforced simulation initialized with the velocity field of the mode. Upper row now depicts the tendency of kinetic energy, rather than wind work (which is zero). Fields are averages over the first 6 days of the integration.

such localized energy dissipation has yet to be confirmed in observations, and its relevance for maintaining abyssal stratification has yet to be established, it is tempting to speculate whether the apparent increase in recurrence frequency for the Central Pacific El-Niño events might have an impact on abyssal mixing in the Southeast Pacific through the excitation of this topographic mode.

Acknowledgments

This research was supported by the Regional and Global Climate Modeling Program of the US Department of Energy Office of Science, and by NSF-OCE award 0928473. Los Alamos National Laboratory is operated by the Los Alamos National Security, LLC for the National Nuclear Security Administration of the U.S. Department of Energy under Contract DE-AC52-06NA25396. The wind stress data used in this study are from the Research Data Archive (RDA) which is maintained by the Computational and Information Systems Laboratory (CISL) at the National Center for Atmospheric Research (NCAR). NCAR is sponsored by the National Science Foundation (NSF). The original data are available from the RDA (<http://dss.ucar.edu>) in dataset number ds744.9.

Constructive comments by Nicole Jeffery (LANL) and two anonymous reviewers are gratefully acknowledged.

Appendix A. Energetics

A.1. Kinetic energy balance

In this appendix, we provide details on the kinetic energy analysis shown in the main text. We start off with a schematic version of the shallow-water (SW) momentum equations used in this study:

$$\frac{\partial \mathbf{u}}{\partial t} + f \mathbf{k} \times \mathbf{u} = -g \nabla \eta - r \mathbf{u} + \frac{\boldsymbol{\tau}}{\rho_0 H}. \quad (\text{A.1})$$

For convenience of notation, we consider the equations in a Cartesian frame, and the friction term is implicitly assumed to represent horizontal viscosity as well. Here, $\boldsymbol{\tau}$ is the wind stress vector, r is the coefficient of bottom friction, g is the gravitational constant, ρ_0 a reference density, and f the Coriolis parameter.

In order to study the energetics of the modal circulation, we decompose the velocity field at each time step in a modal component and a residual: $\mathbf{u} = \mathbf{u}_m + \mathbf{u}_r$. By multiplying Eq. (A.1)

by \mathbf{u}_m and \mathbf{u}_r we obtain two equations describing the energetics of both the modal and non-modal component:

$$T_{mm} = T_{mr} + C_{mm} + C_{mr} + P_m + R_{mm} + R_{mr} + W_m, \quad (\text{A.2a})$$

$$T_{rr} = T_{rm} + C_{rr} + C_{rm} + P_r + R_{rr} + R_{rm} + W_r, \quad (\text{A.2b})$$

where

$$T_{mm} = \frac{1}{2} \rho_0 H \frac{\partial}{\partial t} |\mathbf{u}_m|^2, \quad T_{rr} = \frac{1}{2} \rho_0 H \frac{\partial}{\partial t} |\mathbf{u}_r|^2,$$

$$T_{mr} = -\rho_0 H \mathbf{u}_m \cdot \frac{\partial}{\partial t} \mathbf{u}_r, \quad T_{rm} = -\rho_0 H \mathbf{u}_r \cdot \frac{\partial}{\partial t} \mathbf{u}_m,$$

$$C_{mm} = -\rho_0 H f \mathbf{u}_m \cdot \mathbf{k} \times \mathbf{u}_m, \quad C_{rr} = -\rho_0 H f \mathbf{u}_r \cdot \mathbf{k} \times \mathbf{u}_r,$$

$$C_{mr} = -\rho_0 H f \mathbf{u}_m \cdot \mathbf{k} \times \mathbf{u}_r, \quad C_{rm} = -\rho_0 H f \mathbf{u}_r \cdot \mathbf{k} \times \mathbf{u}_m,$$

$$P_m = -\rho_0 g H \mathbf{u}_m \cdot \nabla \eta, \quad P_r = -\rho_0 g H \mathbf{u}_r \cdot \nabla \eta,$$

$$R_{mm} = -\rho_0 H r |\mathbf{u}_m|^2, \quad R_{rr} = -\rho_0 H r |\mathbf{u}_r|^2,$$

$$R_{mr} = -\rho_0 H r \mathbf{u}_m \cdot \mathbf{u}_r, \quad R_{rm} = -\rho_0 H r \mathbf{u}_r \cdot \mathbf{u}_m,$$

$$W_m = \mathbf{u}_m \cdot \boldsymbol{\tau}, \quad W_r = \mathbf{u}_r \cdot \boldsymbol{\tau}.$$

The terms T denote tendency terms of modal kinetic energy

$$E_{mm} = \frac{1}{2} \rho_0 H |\mathbf{u}_m|^2$$

the residual kinetic energy

$$E_{rr} = \frac{1}{2} \rho_0 H |\mathbf{u}_r|^2$$

and a mixed-mode kinetic energy

$$E_{mr} = \rho_0 H \mathbf{u}_m \cdot \mathbf{u}_r.$$

Terms labeled C , P , R and W represent work done by the Coriolis force, the pressure gradient force, friction, and wind stress. In the continuous representation of the system, work done by the Coriolis force should be zero, so that $C_{mm} = C_{rr} = 0$ and $C_{mr} = -C_{rm}$. For a discretized system, these conditions do not necessarily hold. In particular, for a C-grid discretization the Coriolis force does perform work locally, and although the global integral vanishes, integration over a subdomain will in general not be zero. For the numerical representation of a purely geostrophic flow, the sum of work done by the pressure gradient and the coriolis force should add up to zero, so that $C+P$ reflects the combined work of the Coriolis and pressure gradient forces on the ageostrophic component. In practice, C can be considered as the divergence of a short-range, non-physical energy flux.

In the main paper, the following notation convention is used:

| Main text | Appendix | |
|-----------|----------------------------------|-------|
| E_m | E_{mm} | |
| F_m | $T_{mr} + C_{mm} + C_{mr} + P_m$ | |
| R_m | $R_{mm} + R_{mr}$ | |
| W_m | W_m | (A.3) |
| E_r | E_{rr} | |
| F_r | $T_{rm} + C_{rr} + C_{rm} + P_r$ | |
| R_r | $R_{rr} + R_{rm}$ | |
| W_r | W_r | |

References

Ashok, K., Behera, S.K., Rao, S.A., Weng, H., Yamagata, T., 2007. El Niño modoki and its possible teleconnection. *J. Geophys. Res.* 112.

Atlas, R., Hoffman, R.N., Ardizzone, J., Leidner, S.M., Jusem, J.C., Smith, D.K., Gombos, D., 2011. A Cross-calibrated, multiplatform ocean surface wind

velocity product for meteorological and oceanographic applications. *Bull. Am. Meteorol. Soc.* 92, 157–174.

Atlas, R., Hoffman, R.N., Bloom, S.C., Jusem, J.C., Ardizzone, J., 1996. A multiyear global surface wind velocity data set using SSM/I wind observations. *Bull. Am. Meteorol. Soc.* 77, 869–882.

Boeing, C., Lee, T., Zlotnicki, V., 2011. A record-high ocean bottom pressure in the South Pacific observed by GRACE. *Geophys. Res. Lett.* 38, L04602.

Botta, E.F.F., Wubs, F.W., 1999. MRILU: an effective algebraic multi-level ILU-preconditioner for sparse matrices. *SIAM J. Matrix Anal. Appl.* 20, 1007–1026.

Chao, Y., Fu, L.L., 1995. A comparison between the TOPEX/POSEIDEON data and a global ocean general circulation model during 1992–1993. *J. Geophys. Res.* 100, 24965–24976.

Dijkstra, H.A., De Ruijter, W.P.M., 2001. On the physics of the Agulhas current: steady retroflection regimes. *J. Phys. Oceanogr.* 31, 2971–2985.

Dijkstra, H.A., Molemaker, M.J., 1999. Imperfections of the North-Atlantic wind-driven ocean circulation: continental geometry and wind stress shape. *J. Mar. Res.* 57, 1–28.

Dijkstra, H.A., Öksüzüoğlu, H., Wubs, F.W., Botta, E.F.F., 2001. A fully implicit model of the three-dimensional thermohaline ocean circulation. *J. Comput. Phys.* 176, 685–715.

Dijkstra, H.A., Schmeits, M.J., Katsman, C.A., 1999. Internal variability of the North Atlantic wind-driven ocean circulation. *Surv. Geophys.* 20, 463–503.

van Dorselaer, J.J., 1997. Computing eigenvalues occurring in continuation methods with the Jacobi–Davidson QZ method. *J. Comput. Phys.* 138, 714–733.

Fu, L.L., 2003. Wind-forced intraseasonal sea level variability of the extratropical oceans. *J. Phys. Oceanogr.* 33, 436–449.

Fu, L.L., Cheng, B., Qiu, B., 2001. 25-day period large-scale oscillations in the Argentine Basin revealed by the TOPEX/Poseidon altimeter. *J. Phys. Oceanogr.* 31, 506–517.

Fu, L.L., Smith, R.D., 1996. Global ocean circulation from satellite altimetry and high-resolution computer simulation. *Bull. Am. Meteorol. Soc.* 77, 2625–2636.

Hirose, N., Fukumori, I., Zlotnicki, V., Ponte, R.M., 2001. Modeling the high-frequency barotropic response of the ocean to atmospheric disturbances: sensitivity to forcing, topography, and friction. *J. Geophys. Res.* 106, 30987–30995.

Hughes, C.W., Meredith, M.P., Heywood, K.J., 1999. Wind-driven transport fluctuations through Drake Passage: a Southern Mode. *J. Phys. Oceanogr.* 29, 1971–1992.

Hughes, C.W., Stepanov, V.N., Fu, L.L., Barnier, B., Hargreaves, G.W., 2007. Three forms of variability in Argentine Basin ocean bottom pressure. *J. Geophys. Res.* 112, 1464, <http://dx.doi.org/10.1029/2006JC003679>.

Koblinsky, C.J., 1990. The global distribution of f/H and the barotropic response of the ocean. *J. Geophys. Res.* 95, 3213–3218.

Large, W.G., Pond, S., 1982. Sensible and latent heat flux measurements over the ocean. *J. Phys. Oceanogr.* 12, 464–482.

Lee, T., Hobbs, W.R., Willis, J.K., Halkides, D., Fukumori, I., Armstrong, E.M., Hayashi, A.K., Liu, W.T., Patzert, W., Wang, O., 2010. Record warming in the South Pacific and Western Antarctica associated with the strong Central-Pacific El Niño in 2009–10. *Geophys. Res. Lett.* 37.

Munk, W., 1950. On the wind-driven ocean circulation. *J. Meteorol.* 7, 79–93.

Nowlin, Jr., W.D., 1967. A steady wind-driven, frictional model of two moving layers in a rectangular ocean basin. *Deep-Sea Res. Oceanogr. Abstr.* 14, 89–110.

Polzin, K.L., 2010. Mesoscale eddy-internal wave coupling. Part II: energetics and results from PolyMode. *J. Phys. Oceanogr.* 40, 789–801.

Sleijpen, G.L.G., van der Vorst, H.A., 1996. A Jacobi–Davidson iteration method for linear eigenvalue problems. *SIAM J. Matrix Anal. Appl.* 17, 410–425.

Vivier, F., Kelly, K.A., Harismendy, M., 2005. Causes of large-scale sea level variations in the Southern Ocean: analyses of sea level and a barotropic model. *J. Geophys. Res.* 110, C09014, <http://dx.doi.org/10.1029/2004JC002773>.

Webb, D.J., De Cuevas, B.A., 2002a. An ocean resonance in the Indian sector of the Southern Ocean. *Geophys. Res. Lett.* 29 (14), <http://dx.doi.org/10.1029/2002GL015270>.

Webb, D.J., De Cuevas, B.A., 2002b. An ocean resonance in the Southeast Pacific. *Geophys. Res. Lett.* 29 (8), <http://dx.doi.org/10.1029/2001GL014259>.

Webb, D.J., De Cuevas, B.A., 2003. The region of large sea surface height variability in the Southeast Pacific Ocean. *J. Phys. Oceanogr.* 33, 1044–1056.

Weijer, W., 2008. Normal modes of the Mascarene Basin. *Deep-Sea Res. II* 55, 128–136.

Weijer, W., 2010. An almost-free barotropic mode in the Australian–Antarctic Basin. *Geophys. Res. Lett.* 37, L10602, <http://dx.doi.org/10.1029/2010GL042657>.

Weijer, W., Gille, S.T., Vivier, F., 2009. Modal decay in the Australia–Antarctic Basin. *J. Phys. Oceanogr.* 39, 2893–2909.

Weijer, W., Vivier, F., Gille, S.T., Dijkstra, H., 2007a. Multiple oscillatory modes of the Argentine Basin. Part I: statistical analysis. *J. Phys. Oceanogr.* 37, 2855–2868.

Weijer, W., Vivier, F., Gille, S.T., Dijkstra, H., 2007b. Multiple oscillatory modes of the Argentine Basin. Part II: the spectral origin of basin modes. *J. Phys. Oceanogr.* 37, 2869–2881.